Acta metall. mater. Vol. 41, No. 10, pp. 2985–2992, 1993
Printed in Great Britain.

0956-7151/93 $6.00 + 0.00

EXPERIMENTAL DETERMINATION OF SILICA/COPPER INTERFACIAL TOUGHNESS

M. E. THURSTON and A. T. ZEHNDER
Department of Theoretical and Applied Mechanics, Cornell University, Ithaca, NY 14853-1503, U.S.A.

(Received 18 January 1993)

Abstract—Experiments designed to measure the fracture toughness of ceramic–metal interfaces over a wide range of phase angles are described, and a simple approach to data analysis accounting for plasticity effects in specifying interfacial toughness is outlined. A modified version of a fixture proposed by Richard and Benitz [*Int. J. Fract.* **22**, R55 (1983)] is used to apply mixed-mode loadings to silica/copper sandwich specimens. The experimentally observed crack trajectories depend on the phase angle of loading. In general, the tendency for initial propagation of the crack to occur in the ceramic increases as the magnitude of the phase angle increases. The introduction of a modest amount of mixed-mode loading resulted in a substantial increase in fracture toughness, from approximately 2.2 J/m^2 at 3° to 6.4 J/m^2 at 16° and 8.7 J/m^2 at −10°. The data clearly indicate that plasticity effects become increasingly important as the magnitude of the phase angle increases.

1. INTRODUCTION

Experimental data on mixed-mode fracture toughness of bimaterial interfaces is scarce and for ceramic–metal interfaces is rarer still. Prior to Rice's 1988 review article [2], the significance of the phase angle in specifying fracture toughness was not widely appreciated. Since then, mixed-mode tests over a range of phase angles have been performed on various materials bonded to epoxy [3–5]. For brittle materials like epoxy, data analysis is relatively simple because small-scale yielding (SSY) conditions may be assumed. However, due to combined mechanical and thermal loading, in ceramic–metal systems the metal will in general undergo significant plastic deformation. Although certain specific aspects of ceramic–metal interfaces have been tested [6–9], the difficulty in properly accounting for plasticity effects may explain why a systematic determination of mixed-mode ceramic–metal interfacial toughness for a range of phase angles was until recently [10] lacking in the literature.

As noted by Thouless [11], one possible approach for specifying the fracture toughness of bimaterial interfaces is on a macroscopic level. For example, a crack on the interface of a ceramic–metal system is subjected to a range of mixed-mode loadings and a nominal toughness is inferred from the measured failure loads. The vast majority of the experimental investigations to date have adopted this approach. On a more microscopic scale, however, these experiments indicate that several different crack trajectories are found to occur, depending on the phase angle of loading and other factors. In the present study, each of these fracture patterns is considered to be a distinct failure mode and we are careful to distinguish between the *intrinsic* toughness of the interface, when propagation of the crack occurs, at least initially, along the interface, and the nominal toughness, when the crack propagates from the pre-crack tip immediately into one of the constituent materials.

The purpose of the current work is to describe experiments designed to measure the fracture toughness of ceramic–metal interfaces over a wide range of phase angles, and to outline a simple approach to data analysis accounting for plasticity effects in specifying interfacial toughness. The outline of the remainder of this paper is as follows: the experimental procedure is described and the experimental data are presented in Section 2, a method for extracting the interfacial fracture toughness from the measured quantities is proposed and applied to the experimental data in Section 3, and conclusions and areas for further research are discussed in the final section.

2. EXPERIMENTAL

2.1. Test samples

The samples selected for this study were sandwich specimens consisting of a 0.127 mm thick layer of copper (Cu—material No. 2) foil† hot-pressed between two pieces of fused silica‡ (SiO_2—material No. 1), each 20 × 10 × 3 mm. The relevant constraints on specimen geometry are that the metal layer height, h, be small compared to all other in-plane dimensions, and that the specimen thickness, t, be sufficiently large to allow for valid plane strain fracture toughness measurements. According to ASTM standard E399, this requires that $t \geqslant 2.5$

†Utility Brass and Copper Co., Moonachie, N.J.
‡Esco Products Inc., Oak Ridge, N.J.

$(K_c/\sigma_c)^2$. Hence for $t = 3$ mm, the plane strain assumption is valid for measured $K_c \leqslant 2.0$ MPa $m^{1/2}$; the experimentally determined values are all less than 1.1 MPa $m^{1/2}$. Table 1 summarizes the mechanical properties of the materials used in this study; in particular, note the significant thermal and elastic mismatch typical of ceramic–metal systems.

Sample preparation, depicted schematically in Fig. 1, proceeded as follows [12]: first, the Cu foil and SiO_2 pieces were cleaned successively in (1) a solution of 25% petroleum ether, 75% water at 60–80°C with ultrasonic agitation, (2) a solution of 10% nitric acid, 90% ethanol with ultrasonic agitation, and (3) hot water, and allowed to air dry. The SiO_2 pieces were then heat-treated at 1000°C for 3 h in air, so as to remove any residual hydrocarbons remaining on the specimen surface. For each sample, two thin films were evaporated onto the bonding surface of one of the SiO_2 pieces: a film of carbon across a portion of the length of the surface, followed by a film of copper across the entire length. The carbon film does not bond to the copper, creating a pre-crack of the desired length. The choice of carbon is arbitrary; any material with a high enough melting temperature relative to copper, e.g. platinum, will also work as a masking material. The evaporated copper film facilitates bonding between the Cu and SiO_2, resulting in stronger, more consistent bonds. On the bonding surface of the second SiO_2 piece, a thin film of chromium was evaporated so as to confine crack propagation to the (weaker) SiO_2/Cu interface. The Cu foil was then placed between the two SiO_2 pieces in a graphite die and the sample was hot-pressed under vacuum ($\leqslant$0.010 mm Hg) at 1000°C for 4 h under a uniaxial compressive stress of 14.8 MPa (Fig. 2). Of the processing variables, the most significant parameter affecting the strength of the resulting bond is temperature—we found about 90% of the metal melting temperature to be optimal. The time can then be varied to control the strength of the resulting bond.

Table 1

Material property	Fused silica	99.9% OFHC copper
Young's modulus, E (GPa)	69.6[a]	113.5
Shear modulus, μ (GPa)	29.7	42.2[b]
Poisson's ratio, ν	0.17[a]	0.345[c]
Therm. exp. coeff. ($\times 10^{-6}$/°C)	0.51[a]	16.75[c]
Yield stress, σ_0 (MPa)	—	60.0[d]
Power-law const, $\bar{\alpha}$	—	1.5[e]
Power-law hardening exp, n	—	3.3[e]
Dundurs parameter, α		−0.29
Dundurs parameter, β		−0.17
Bimaterial const., ϵ		0.055

[a]Esco Products, Inc., Moonachie, N.J.
[b]P. S. Follansbee and G. T. Gray III, Dynamic deformation of shock prestrained copper, *Materials Science and Engineering*, **A138** (1991).
[c]S. H. Crandall, N. C. Dahl and T. J. Lardner, *An Introduction to the Mechanics of Solids*. McGraw-Hill, New York (1978).
[d]K. K. Chawla, *Composite Materials*. Springer, Berlin (1987).
[e]T. Weerasooriya and R. A. Swanson, U.S. Army Materials Laboratory Report MTL TR 91-20 (1991).

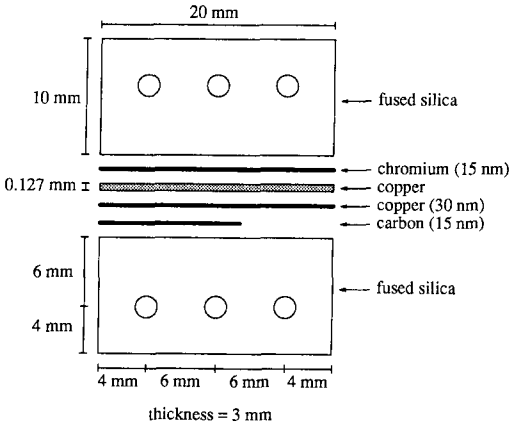

Fig. 1. Schematic of test specimen preparation.

2.2. Test procedure

The finished samples were loaded in a universal testing machine using a steel loading fixture, which allows the angle of the remotely applied load to be varied over the range $-90° < \Theta < 90°$ in 15° increments (Figs 3–5). Note that the slotted bolt holes fix the directions of the loads applied to the sample by the fixture, allowing their magnitudes to be calculated from static equilibrium [13]. After calibration of the testing machine, the samples were loaded to failure at a constant cross-head speed of 0.04 cm/min, and the maximum (failure) load was recorded. The magnitude of the crack opening displacement, which may be estimated from an asymptotic analysis to be on the order of 3 μm, is too small to be measured conveniently. Therefore, instead of calculating the J-integral from load–displacement curves, the method described in the next section is used to estimate J as a function of the measured load.

2.3. Observations

Crack propagation was observed to be unstable in all cases. Adopting the sign convention that a loading

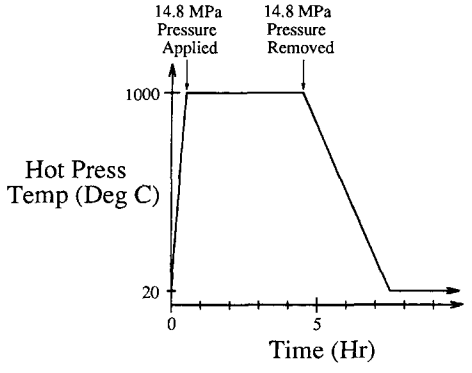

Fig. 2. Temperature vs time during bonding.

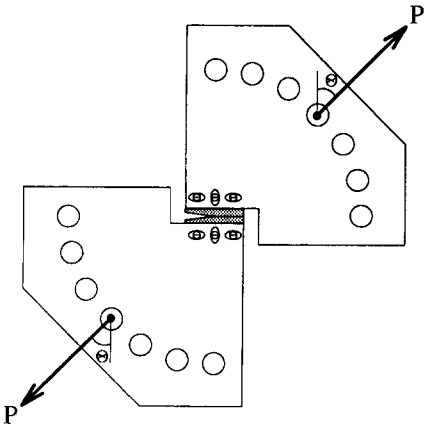

Fig. 3. Mixed-mode loading fixture.

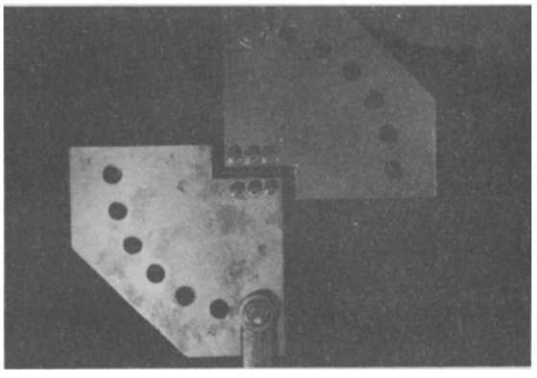

Fig. 5. Test fixture and sample.

with mode-II component acting to the right on the upper crack face corresponds to a positive phase angle of loading, we find that in seeking a local mode-I trajectory, for positive phase angle cracks have a strong tendency to kink into the ceramic. For negative phase angles, the high toughness of the metal tends to promote interface fracture, except that for large negative phase angles fracture is observed to occur in the ceramic before the interfacial toughness is reached. From examination of the fracture surfaces, the qualitative fracture behavior may be classified into four categories (Fig. 6). For negative and small positive (i.e. nominally mode I) load phase angles, cracks typically propagated along the interface for a short distance, then deviated into the ceramic to a depth of less than 1 mm and propagated parallel to the interface across the remaining ligament (type I_A). For one sample the behavior was similar except that the crack propagated from the pre-crack tip directly into the ceramic (type I_B). For larger positive load phase angles, the majority of cracks propagated from the pre-crack tip directly into the ceramic, typically at an angle of slightly lesser magnitude than the load angle (type II_B). A fewer number propagated along the interface for a short distance before branching into the ceramic (type II_A). Hence, according to our terminology, type A fracture patterns represent intrinsic interfacial toughness measurements, while type B patterns represent nominal interfacial toughness measurements. One sample loaded at $-45°$ and two at $-30°$ fractured in the ceramic at the bolt holes prior to interface fracture. The results of twenty samples loaded at angles from $-45°$ to $+60°$ which failed at the interface are summarized in Table 2. For each sample, the last column lists the fracture pattern type, and either the measured length of crack propagation along the interface in the intrinsic case, or the measured initial propagation angle into the ceramic in the nominal case.

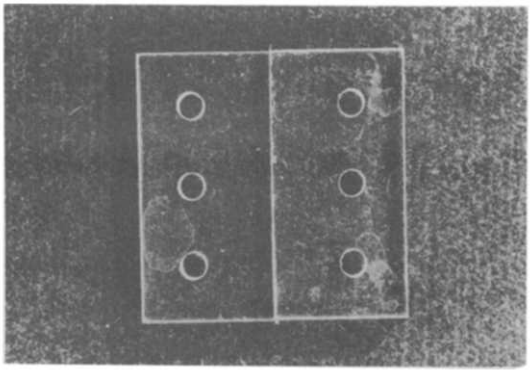

Fig. 4. Hot-pressed test specimen.

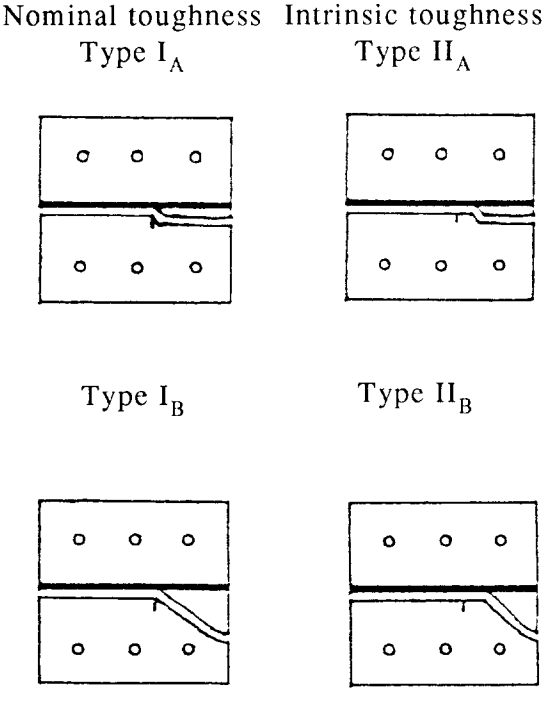

Fig. 6. Observed crack trajectories.

Table 2

Test No.	$\Theta(^\circ)$	P_{max}(N)	Crack path
1	−45	92.96	I_A/1.0 mm
2	−45	83.80	I_A/0.5 mm
3	−30	67.95	I_A/1.0 mm
4	−30	73.39	I_A/1.0 mm
5	−30	54.49	I_A/0.5 mm
6	0	40.08	I_A/0.5 mm
7	0	24.69	I_A/3.5 mm
8	0	22.24	I_A/2.5 mm
9	0	30.51	$I_B/<-10°$
10	+15	37.90	II_A/4.0 mm
11	+15	52.93	II_A/1.0 mm
12	+15	24.24	$II_B/-10°$
13	+30	56.58	II_A/1.5 mm
14	+30	58.18	II_A/0.5 mm
15	+30	54.93	$II_B/-20°$
16	+45	61.29	$II_B/-50°$
17	+45	68.59	$II_B/-40°$
18	+45	72.10	$II_B/-30°$
19	+60	75.13	$II_B/-50°$
20	+60	82.82	$II_B/-45°$

Cross-head speed: 0.04 cm/min.

Surface profile meaurements using an Alpha-step profilometer were performed on the silica and copper surfaces prior to bonding and after fracture. Compared to the surface before bonding, the copper surface after fracture was approximately five times rougher, indicative of significant local plastic deformation in the vicinity of the crack tip. In comparison, the silica surface roughness was relatively unaffected. However, the initial roughness of the silica bonding surface may significantly influence the mixed mode fracture toughness, as will be discussed briefly at the end of the next section.

3. DATA REDUCTION AND ANALYSIS

A fundamental aim of fracture mechanics is to uniquely determine the stress state at the tip of a crack in a body, given only the applied loading and system geometry, i.e. quantities which can be measured experimentally. The goal of this chapter, therefore, is to extract the interfacial fracture toughness from the load and geometry data presented in Table 2 and Fig. 1. The first step towards this goal is a definition of interfacial toughness incorporating the relevant elastic mismatch and plasticity effects.

3.1. *Definition of interfacial toughness*

The inherent coupling of tensile and shear modes at bimaterial interfaces has important implications for the specification of interfacial fracture toughness. In order to circumvent the ambiguity associated with the bimaterial stress intensity factor, $\mathcal{K}$, the mode mixity may be specified relative to a fixed material length, $\hat{L}$

$$\tan\hat{\phi} = \left(\frac{\sigma_{xy}}{\sigma_{yy}}\right)_{\theta=0,r=\hat{L}} = \frac{\mathrm{Im}\{\mathcal{K}\hat{L}^{i\epsilon}\}}{\mathrm{Re}\{\mathcal{K}\hat{L}^{i\epsilon}\}} \quad (1)$$

where the bimaterial parameter, ϵ, is given by

$$\epsilon = \frac{1}{2\pi}\ln\left(\frac{1-\beta}{1+\beta}\right) \quad (2)$$

and the Dundurs parameters, α and β, are given by

$$\alpha = \frac{\bar{E}_1 - \bar{E}_2}{\bar{E}_1 + \bar{E}_2}, \quad \beta = \frac{1}{2}\left[\frac{\mu_1(1-2\nu_2) - \mu_2(1-2\nu_1)}{\mu_1(1-\nu_2) + \mu_2(1-\nu_1)}\right], \quad (3)$$

where $\bar{E} = 2\mu/(1-\nu)$ for plane strain. A logical choice for $\hat{L}$ falls inside the $\mathcal{K}$-annulus, i.e. the region at distances large compared to the fracture process zone, but small compared to L, the characteristic length.

For sandwich geometries like the specimen in this study, where the thickness of the middle layer is small compared to the other dimensions of the sample, the stress fields at the tip of an interface crack are similar to those for the corresponding homogeneous problem. In particular, the stresses sufficiently remote from the interface crack tip will not be affected by the presence of the layer. By equating energy release rates per unit of crack advance along the interface in the remote and near-tip regions, Suo and Hutchinson [14] derived a universal relation between the actual stress intensity factors, $Ke^{i\psi} = K_1 + iK_2$ characterizing the near field of the interface crack, and the stress intensity factors, $K^\infty e^{i\phi} = K_1 + iK_{II}$ for the corresponding homogeneous problem (the remote field for the sandwich problem). With respect to the remote-field stress intensity factor, the complex near-tip stress intensity factor so derived has magnitude scaled by a factor $p = \sqrt{(1-\alpha)/(1-\beta^2)}$, and phase angle shifted by ω, a non-dimensional function of the Dundurs parameters. Incorporating this effect, sometimes referred to as elastic shielding, the near-tip elastic phase angle becomes

$$\hat{\psi} = \psi + \epsilon\ln\left(\frac{\hat{L}}{L}\right) = \phi + \omega + \epsilon\ln\left(\frac{\hat{L}}{L}\right) = \hat{\phi} + \omega. \quad (4)$$

Parameters uniquely specifying bimaterial crack tip fields when one or both of the materials deforms plastically have yet to be determined. Based on finite element calculations, Shih and co-workers [15] have recently proposed, by analogy with the parameters J and M_p for the mixed mode HRR fields, that under SSY conditions bimaterial crack tip fields be parameterized by the J-integral and a near-tip plastic phase angle, ξ, given by

$$\xi = \hat{\psi} + \epsilon\ln\left(\frac{K^2}{\sigma_0^2\hat{L}}\right). \quad (5)$$

This form for ξ may be determined either from dimensional analysis or analytically by solving an elasticity problem [16]. Note that, consistent with the finite element results, the phase angle, ξ, changes as the magnitude of the load, i.e. K, increases, but is independent of distance, r. A limitation of the proposed parameterization is that its regime of validity may be confined to small phase angles ($|\xi| < \pi/6$). Let D be the characteristic size of the region near the crack tip where the elastic strains are negligible compared to the plastic strains. If the characteristic

dimension of the fracture process zone, R, is small compared to D, then fracture initiation is controlled by the deformation in the J-dominant region, $R < r < D$. The interfacial fracture toughness is then uniquely specified by J reaching a critical value

$$J = J_c(\xi). \tag{6}$$

3.2. Method for approximation of J-integral

The engineering approach to elastic–plastic fracture [17, 18] approximates the J-integral over the complete range of yield behavior by calculating J for SSY and fully-plastic conditions, and superimposing them according to

$$J = J_e + J_p. \tag{7}$$

In the procedure described below, the development of Kanninen and Popelar [19] for homogeneous materials is extended to the bimaterial case.

3.2.1. Plastic regime. For the plastic behavior of the metal, power-law hardening is assumed such that under uniaxial load

$$\frac{\gamma}{\gamma_b} = \bar{\alpha}\left(\frac{\sigma}{\sigma_o}\right)^n \tag{8}$$

where stress and strain are denoted by σ and γ, σ_0 is the yield stress, $\gamma_0 = \sigma_0/E$, and $\bar{\alpha}$, n for copper are given in Table 1. Adopting a small-strain, J_2 deformation theory of plasticity, equation (8) may be generalized as follows

$$\frac{\gamma_{ij}}{\gamma_0} = \tfrac{3}{2}\alpha\left(\frac{\sigma_e}{\sigma_0}\right)^{n-1}\frac{S_{ij}}{\sigma_0} \tag{9}$$

where

$$\sigma_e = \sqrt{\tfrac{3}{2}S_{ij}S_{ij}}, \tag{10}$$

$$S_{ij} = \sigma_{ij} - \tfrac{1}{3}\sigma_{kk}\delta_{ij}. \tag{11}$$

Here δ_{ij} is the Kronecker delta and the summation convention applies to repeated indices. Recall that the loading fixture is designed so that the directions of the tractions applied to the specimen remain fixed, with magnitudes linearly proportional to a single load parameter P, e.g. $T_i = P\hat{T}_i$. Under such loading conditions, for materials obeying (9) J_p takes the particularly simple form [20]

$$J_p = \sigma_0\gamma_0\bar{\alpha}b\left(\frac{P}{P_0}\right)^{n+1}\hat{J}_p[a/w, n], \tag{12}$$

where P_0 is the limit load based on σ_0, b is the uncracked ligament length, a is the crack length, w is the specimen width, and $\hat{J}_p$ is dimensionless and independent of P. A derivation of (12) is given in [21].

3.2.2. Elastic regime. Under SSY conditions, J_e is related to the stress intensity factors by [22]

$$J_e = J_e(a_e) = (1-\beta^2)\frac{K^2}{E^*} \tag{13}$$

where, for plane strain

$$\frac{1}{E^*} = \frac{1}{2}\left(\frac{1}{\bar{E}_1} + \frac{1}{\bar{E}_2}\right) \tag{14}$$

and

$$K = pK^\infty = \sqrt{\frac{1-\alpha}{1-\beta^2}(K_I^2 + K_{II}^2)} \tag{15}$$

$$K_I = F_I\frac{P}{wt}\sqrt{\pi a_e}, \quad K_{II} = F_{II}\frac{P}{wt}\sqrt{\pi a_e} \tag{16}$$

where F_I and F_{II} are dimensionless functions of geometry, and the Irwin-type effective crack length, a_e is given by

$$a_e = a + \Phi r_y \tag{17}$$

$$\Phi = \frac{1}{\left[1 + \left(\frac{P}{P_0}\right)^2\right]} \tag{18}$$

$$r_y = \frac{1}{6\pi}\left(\frac{n-1}{n+1}\right)\left(\frac{K}{\sigma_0}\right)^2. \tag{19}$$

For simplicity K in the expression for r_y is calculated using a in place of a_e in (16). The coefficient Φ is designed to reduce the effective crack length

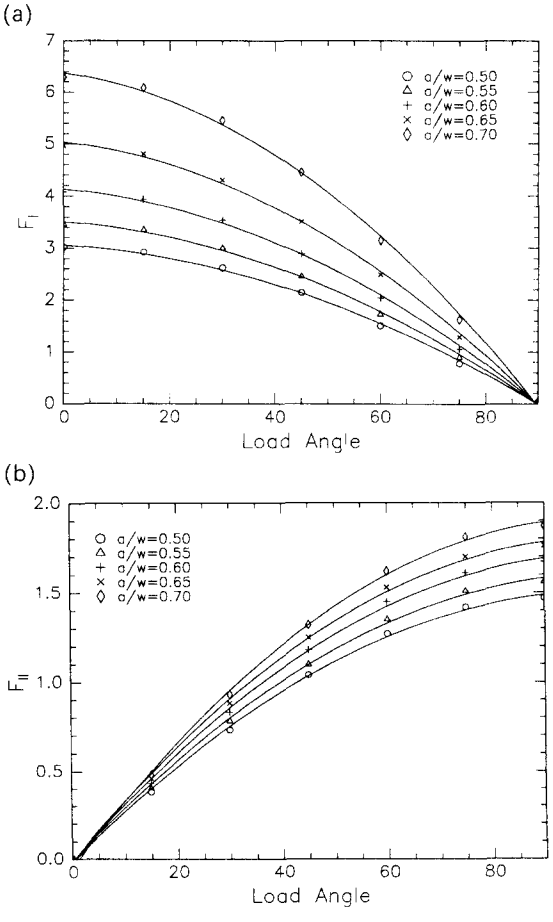

Fig. 7. (a) Mode I SIF vs load angle. (b) Mode II SIF vs load angle.

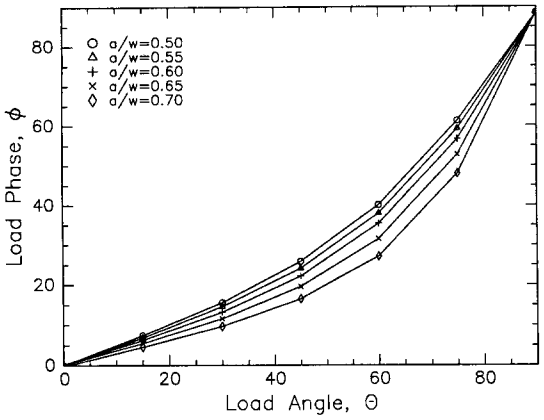

Fig. 8. Load phase vs load angle.

correction term in the LSY regime where the J_p term dominates.

3.2.3. Stress intensity calibration. Determination of the non-dimensional functions F_I, F_{II}, and $\hat{J}_p$, was performed using the finite element method. The results for F_I and F_{II} are plotted as a function of load angle and crack length in Fig. 7. Once the F's, and hence the K's, are known, the relationship between the angle of the applied load, Θ, and the remote load phase angle, ϕ, is completely determined (Fig. 8). Together, the elastic and plastic calibrations, through equations (13)–(19) and (12), relate J directly to the applied load, P. The J vs load behavior is plotted for remote load angles, $\Theta = 0°$ and 60°, and the relevant crack length, $a/w = 0.6$, in Fig. 9. For a fixed load the plastic component of J is seen to increase with increasing phase angle magnitude.

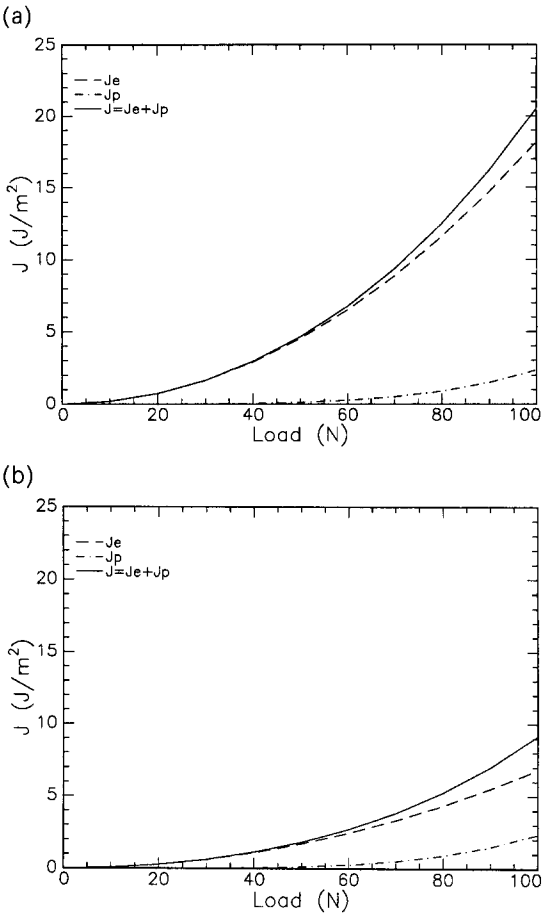

Fig. 9. (a) J vs load. Load angle = 0. (b) J vs load. Load angle = 60.

3.3. Data analysis

The reduced data are summarized in Table 3, in which the choice $\hat{L} = L = h$, the copper foil thickness, is made for simplicity, such that by equation (4), $\hat{\psi} = \psi = \phi + \omega$. In the last column, the characteristic dimension of the plastic zone is estimated as $r_p = \Lambda(\xi)(K/\sigma_0)^2$, by linearly interpolating the dimensionless parameter Λ between $\Lambda = 0.15$ at $\xi = 0°$ and $\Lambda = 0.70$ at $\xi = 90°$ [15]. Taking as a rule of thumb estimate that $r_p/L \leqslant 0.35$ for the SSY assumption to hold, the plastic zone sizes for all but the first and last four tests fall within this regime.

Table 3

No.	Θ (°)	$\hat{\phi}$ (°)	$\hat{\psi}$ (°)	K (MPa$\sqrt{\text{m}}$)	J_e (J/m^2)	J_p (J/m^2)	J (J/m^2)	ξ (°)	Λ	r_p (μm)
1	−45	−22	−19	1.08	12.29	1.77	14.06	−19	0.27	87
2	−45	−22	−19	0.97	9.98	1.13	11.11	−19	0.27	71
3	−30	−13	−10	0.91	8.82	0.45	9.27	−10	0.21	48
4	−30	−13	−10	0.99	10.39	0.64	11.03	−10	0.21	57
5	−30	−13	−10	0.74	5.72	0.18	5.90	−10	0.21	32
6	0	0	3	0.61	3.90	0.05	3.95	3	0.17	18
7	0	0	3	0.37	1.48	0.01	1.49	3	0.17	6
8	0	0	3	0.34	1.20	0.00	1.20	3	0.17	5
9	0	0	3	0.46	2.26	0.01	2.27	3	0.17	10
10	15	6	9	0.56	3.29	0.04	3.33	9	0.21	18
11	15	6	9	0.78	6.43	0.16	6.59	9	0.21	35
12	15	6	9	0.36	1.35	0.00	1.35	9	0.21	8
13	30	13	16	0.76	6.16	0.21	6.37	16	0.25	40
14	30	13	16	0.79	6.52	0.24	6.76	16	0.25	43
15	30	13	16	0.74	5.81	0.18	5.99	16	0.25	38
16	45	22	25	0.71	5.33	0.30	5.63	25	0.30	42
17	45	22	25	0.80	6.68	0.48	7.16	25	0.30	53
18	45	22	25	0.84	7.38	0.59	7.97	25	0.30	59
19	60	35	38	0.70	5.15	0.71	5.86	38	0.38	52
20	60	35	38	0.77	6.26	1.08	7.34	38	0.38	63

$\hat{L} = h = 127\ \mu$m.

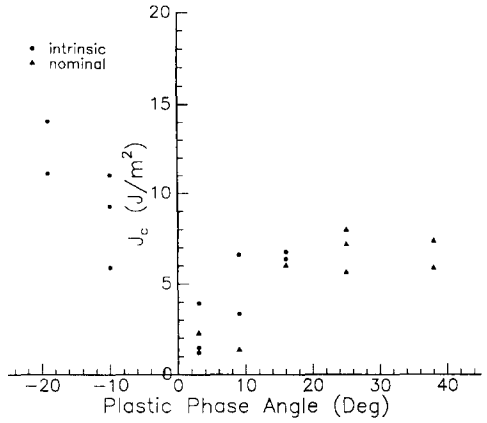

Fig. 10. Fracture toughness vs mixity.

The fracture toughness as a function of mixity is plotted in Fig. 10. Making use of the crack path in Table 2, the intrinsic and nominal toughness values have been labeled accordingly. Note that the nominal toughness values represent a lower bound on the intrinsic fracture toughness for that sample. Judging from the limited mixed-mode interfacial data in the literature, the scatter in the data for multiple samples at the same phase angle, while significant, appears typical. Perhaps the most striking result is the substantial increase in toughness with only a moderate increase in mixity, approximately three-fold between $\xi = 3°$ and 16° and four-fold between $\xi = 3°$ and $-10°$. To our knowledge, the current data are the first mixed-mode SiO_2/Cu toughness data in the literature, making meaningful comparison difficult. However, the nominal mode-I toughness values reported for soda-lime glass/copper interfaces by Oh *et al.* [6], $0.35 < K_c < 0.42$ Mpa m$^{1/2}$, fall within the range of the corresponding values ($\xi = 3°$) measured here.

Clearly, asymmetry of the stress distribution and plastic shielding contribute to the phase dependence of the toughness; whether other factors also contribute is still an open question [23]. The theoretically predicted smoothness of the interface in that study may underestimate the actual roughness, which we suspect may account for at least part of the reported discrepancy between the measured and calculated mixed-mode toughness behavior. To examine the influence of surface roughness in the current measurements, we also consider the simplified (elastic, homogeneous, frictionless) model of Evans and Hutchinson [24], which relates the increase in critical energy release rate with increasing mode mixity to a single material behaviour, χ, given by

$$\chi = \frac{EH^2}{G_0 L} \tag{20}$$

where H is the amplitude of the interface roughness, L is the wavelength, G_0 is the adhesive energy of the interface, and E is Young's modulus. Here $E = 69.6$ MPa, $G_0 \approx 2.0$ J/m^2, the amplitude of the interface roughness is approximated by the rms amplitude of the silica surface profile measurements prior to bonding as $H = 0.18\,\mu$m, with wavelength $L \approx 0.14$ mm. Substituting, we find $\chi \approx 8$, very close to the value which Evans and Hutchinson found to give good agreement between theory and experiment and their glass/epoxy system.

4. CONCLUSIONS

In summary, experiments are described wherein a range of mixed-mode loadings are applied to ceramic–metal sandwich specimens in order to determine the interfacial fracture toughness of a representative fused silica/copper system. In the presence of thermally and mechanically induced plasticity, the fracture toughness is defined in terms of the J-integral reaching a critical value, which in turn depends on a plastic phase angle, ξ, indicating the ratio of shear to normal stress acting on the interface directly ahead of the crack tip. The engineering approach to elastic–plastic fracture of Shih and Hutchinson is extended to the bimaterial case in order to extract the toughness from the measured load and geometry data.

The experimental approach described here for determining interfacial fracture toughness possesses a number of advantageous features. For the sandwich-type specimen geometry, an analytical solution exists relating the bimaterial stress intensity factors (SIF's) to those for the corresponding homogeneous problem, reducing the elastic calibration of the bimaterial SIF's to the simpler task of calibrating the corresponding homogeneous SIF's. Furthermore, the given specimen geometry has the desirable property that the shift in phase of the near-tip stresses with respect to the phase of the far-field stresses is small at most angles, so that the fracture toughness as a function of mixity may in principle be determined over the complete range of phase angles, $-90° < \xi < 90°$. Finally, the choice of the sandwich specimen geometry is designed to minimize, to the extent possible, the influence of residual stresses on the interfacial toughness.

As noted in the introduction, the difficulty in properly accounting for the influence of metal plasticity has long stood as a conceptual stumbling block to the measurement of ceramic-metal interfacial toughness. Here a simple approach to data analysis accounting for plasticity due to mechanical loading has been proposed. This approach would certainly seem justified for ceramic–metal systems for which the thermal mismatch is small. In the general case, the possibility that residual thermal stresses will invalidate the basis for a K-dominant region must be investigated. Work is currently underway on combining the measured experimental data with a finite element model of the stress distribution due to both hot-pressing and the applied mechanical loading, in

order to assess the validity of the engineering approximation and verify that the residual stress effects may safely be neglected.

Large-scale yielding at ceramic–metal interfaces is to be expected in general, due to the ductility of the metal constituent and the combined effects of thermal and elastic mismatch. The current system is atypical in this respect, because of the extremely low toughness of the SiO_2 ($K_c = 0.67$ MPa $m^{1/2}$ [25]). Note that the plastic contribution to the overall J does not exceed 15% for any of the measurements presented in Table 3. For this material system, data reduction based on an elastic analysis would apparently have been adequate, except perhaps for the higher phase angles. Similarly, the choice of phase angle for specifying the toughness data is not critical in this instance, as the phase angles $\hat{\phi}$, $\hat{\psi}$, and ξ differ by no more than 3° in all cases. The data clearly indicate, even for the current material combination, that plasticity effects become increasingly important with increasing phase angle magnitude.

As noted in Section 2, for positive load phase angles, the positive local mode-II component tends to drive a crack on the interface into the ceramic. The explanation for the observed behavior here and in [10], that the crack sometimes propagates immediately into the ceramic and sometimes along the interface for some distance first, is still unclear. The flaw distribution in the ceramic at the interface is one possibility [26], but the current data are insufficient to determine if the distance propagated along the interface prior to encountering a ceramic flaw is Weibull distributed.

As a practical matter, perhaps the most important result of the observed crack path behavior is that the range of phase angles for which the intrinsic toughness governs the fracture behavior of the bimaterial system is limited when the interfacial toughness is comparable in magnitude to that of one of the constituent materials. Stout *et al.* [10] reached a similar conclusion in their four-point bend tests on alumina/niobium systems. We argue that this is a general result for ceramic–metal systems as follows: on the most basic level, metals derive their ductility from the loosely held electrons characteristic of metallic bonds. Ceramics are brittle due to the more tightly held electrons associated with bonds that are typically partly ionic and partly covalent. Because ceramic–metal bonds are ionic, ceramic-metal toughness should be brittle, i.e. it should more closely parallel the fracture behavior of its ceramic rather than metal constituent.

Acknowledgement—The authors gratefully acknowledge the support of the MRL Program of the National Science Foundation under Award No. DMR-9121654.

REFERENCES

1. H. A. Richard and K. Benitz, *Int. J. Fract.* **22,** R55 (1983).
2. J. R. Rice, *J. appl. Mech.* **55,** 98 (1988).
3. H. C. Cao and A. G. Evans, *Mech. Mater.* **7,** 295 (1989).
4. J. S. Wang and Z. Suo, *Acta metall. mater.* **38,** 1279 (1990).
5. K. M. Liechti and Y.-S. Chai, *J. appl. Mech.* **58,** 680 (1991).
6. Tae Sung Oh, R. M. Cannon and R. O. Ritchie, *J. Am. Ceram. Soc.* **70,** C352 (1987).
7. T. S. Oh *et al.*, *Acta metall.* **36,** 2083 (1988).
8. I. E. Reimanis *et al.*, *Acta metall. mater.* **38,** 2645 (1990).
9. A. Bartlett, A. G. Evans and M. Ruehle, *Acta metall. mater.* **39,** 1579 (1991).
10. M. G. Stout, N. P. O'Dowd and C. F. Shih, in *Experiments in Micromechanics of Failure Resistant Materials*, Vol. 130, pp. 9–15. ASME AMD (1991).
11. M. D. Thouless, *Acta metall. mater.* **38,** 1135 (1990).
12. F. P. Bailey and K. J. T. Black, *J. Mater. Sci.* **13,** 1045 (1978).
13. H. A. Richard, *VDI Forsch.* **631,** 1 (1985).
14. Zhigang Suo and J. W. Hutchinson, *Mater. Sci. Engng* **107,** 135 (1989).
15. C. F. Shih, R. J. Asaro and N. P. O'Dowd, *J. appl. Mech.* **58,** 450 (1991).
16. E. Zywicz and D. M. Parks, *J. appl. Mech.* **56,** 577 (1989).
17. C. F. Shih, in *Mechanics of Crack Growth*, pp. 3–26. ASTM STP 590 (1976).
18. C. F. Shih and J. W. Hutchinson, *J. engng Mater. Techn.* **98,** 289 (1976).
19. M. F. Kanninen and C. H. Popelar, *Advanced Fracture Mechanics*. Oxford University Press (1985).
20. N. L. Goldman and J. W. Hutchinson, *Int. J. Solids Struct.* **11,** 575 (1975).
21. M. E. Thurston, Master's thesis, Cornell Univ. (1992).
22. N. P. O'Dowd, C. F. Shih and M. G. Stout, *Int. J. Solids Struct.* **29,** 571 (1992).
23. K. M. Liechti and Y.-S. Chai, *J. appl. Mech.* **59,** 295 (1992).
24. A. G. Evans and J. W. Hutchinson, *Acta metall.* **37,** 909 (1989).
25. J. J. Mecholsky, R. W. Rice and S. W. Freiman, *J. Am. Ceram. Soc.* **57,** 440 (1974).
26. B. J. Dalgleish, M. C. Lu and A. G. Evans, *Acta metall.* **36,** 2029 (1988).